

Ag₂ZnSnS₄ Nanocrystals Expand the Availability of RoHS Compliant Colloidal Quantum Dots

Avijit Saha, Alberto Figueroba, and Gerasimos Konstantatos*



Cite This: *Chem. Mater.* 2020, 32, 2148–2155



Read Online

ACCESS |



Metrics & More

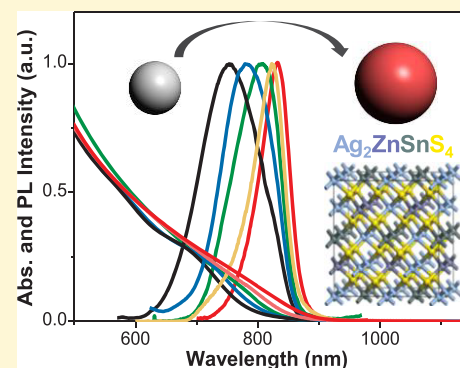


Article Recommendations



Supporting Information

ABSTRACT: The demonstration of the quantum confinement effect in colloidal quantum dots (QDs) has been extensively studied and exploited mainly in Pb and Cd chalcogenide systems. There has been an urgent need recently for the development of non(less)-toxic colloidal QDs to warrant compliance with current safety regulations (Restriction of Hazardous Substances (RoHS) Directive 2002/95/EC). Herein, we report Pb/Cd-free, solution processed luminescent Ag₂ZnSnS₄ (AZTS) colloidal QDs. We present a selective and controlled amine and thiol-free synthesis of air stable luminescent AZTS QDs by the hot injection technique. By controlling the reaction conditions we obtain controlled size variation and demonstrate the quantum confinement effect that is in good agreement with the theoretically calculated values. The band gap of the AZTS QDs is size-tunable in the near-infrared from 740 to 850 nm. Finally, we passivate the surface with Zn-oleate, which yields higher quantum yield (QY), longer lifetime, and better colloidal stability.



INTRODUCTION

Metal chalcogenide colloidal quantum dots (CQDs) have been extensively studied and employed in a number of applications including light emitting diodes, photodetectors, and photovoltaics. In particular, cadmium and lead-based chalcogenide CQDs have been investigated widely and demonstrated efficient optoelectronic device application.^{1–3} Yet, the requirements toward Restriction of Hazardous Substances (RoHS) compliant materials in industry have motivated recent research toward environmentally friendly low-cost-material-based optoelectronic devices.^{4–10} However, in most of these reported materials, such as indium-based phosphides^{8,11} and chalcogenides,^{5–7,9,12} their band gap tunability has been demonstrated mainly across the visible spectrum, and the scarcity of indium may prevent their widespread commercial adoption.

For photovoltaic or biomedical imaging applications, the expansion in the near-infrared is highly desired. Kesterite Cu₂ZnSnS₄ (CZTS) NCs have been extensively studied, yet the demonstration of light emission, band gap tunability, and their successful use in optoelectronic devices has thus far remained elusive. Moreover, the synthetic routes employed for the synthesis of kesterite NCs have been based on amines or thiols as ligands,^{13–15} impeding efficient ligand exchange^{16,17} and their application in optoelectronic devices. For this reason, a synthetic strategy is urgently needed for such NCs to overcome the reliance on amine or thiols. An additional issue of the CZTS compound is the well-known antisite disordering^{18,19} that arises due to the similar ionic size of Cu⁺ (78 pm) and Zn²⁺ (74 pm) and has been responsible for the formation of defects, the presence of band tailing, the poor photo-

luminescence (PL) emission, and the low open circuit voltage (V_{oc}) in solar cells.^{19,20} By replacing Cu⁺ with Ag⁺ (115 pm) antisite disordering can be drastically suppressed in Ag₂ZnSnS₄ compared to Cu₂ZnSnS₄.²¹ AZTS has been reported recently in bulk thin film solar cells as a promising solar absorber.²² Therefore, AZTS is a promising candidate as a RoHS compliant colloidal quantum dot system. Synthesis of AZTS QDs has thus far not been reported except for one report on large sized (15 nm) AZTS nanoparticles.²³ Moreover, size tunable optical absorption and photoluminescence due to the quantum confinement effect has so far not been observed in these quaternary QDs. Nishi et al. have reported size tunable optical absorption in CZTS QDs, however in the absence of PL emission.²⁴ Herein, we report for the first time the synthesis of amine and thiol-free luminescent AZTS colloidal QDs with size tunable band gap akin to their quantum confined nature.

EXPERIMENTAL METHODS

Materials. Silver acetate (AgOAc) 99.99%, tin(II) acetate (Sn(OAc)₂), zinc(II) acetate, dihydrate (Zn(OAc)₂·2H₂O), 98%, oleic acid (OA, 90%), 1-octadecene (ODE, 90%), sulfur powder (99.5%), and hexamethyldisilathiane (HMS) were purchased from Sigma-Aldrich. All these chemicals were used without further

Received: December 27, 2019

Revised: February 6, 2020

Published: February 6, 2020

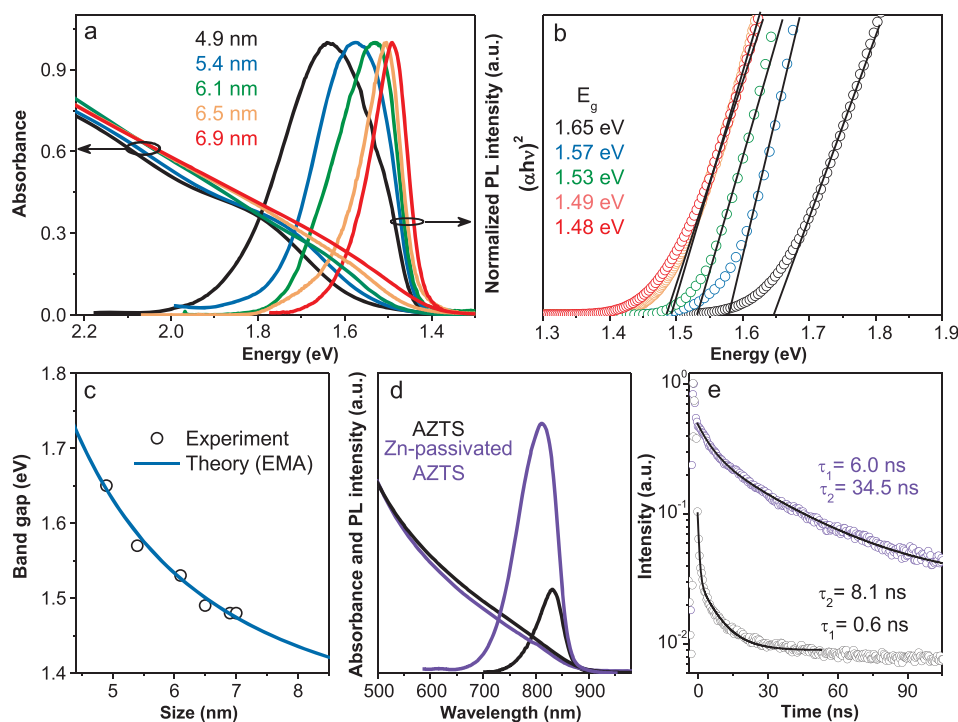


Figure 1. (a) Absorption spectra of AZTS QDs and their corresponding PL spectra overlaid. Note: The apparent spectral narrowing of the PL in larger sized dots is due to reaching the cutoff of the silicon detector. (b) Band gaps determined from the Tauc plot. (c) Variation of the experimentally observed band gaps (open circles) as a function of the QD sizes and a comparison with the theoretically calculated band gap values through effective medium approximation (EMA) approach (blue lines). (d) UV-vis absorption, PL, and (e) PL lifetime of pristine AZTS (black) and Zn-oleate passivated AZTS QDs (violet). The excitation wavelength used both for PL (a, d) and lifetime measurements (e) was 405 nm, and the lifetimes were monitored at the respective peak positions.

purification. HMS is a toxic and malodorous colorless liquid, must be handled using appropriate protective equipment to avoid physical contact, and should be stored in a dry and well ventilated place.

Synthesis of AZTS Nanocrystals. In a typical synthesis, 0.7 mmol of $\text{Ag}(\text{OAc})$, 0.5 mmol of $\text{Zn}(\text{OAc})_2 \cdot 2\text{H}_2\text{O}$, 0.5 mmol of $\text{Sn}(\text{OAc})_2$, and 10 mL of OA were taken in a 50 mL three necked round-bottom flask equipped with a temperature controller probe and connected to a Schlenk line. This reaction mixture was degassed under vacuum for 90 min at 50 °C under constant stirring. The flask environment was switched to argon, and the temperature was raised to the desired temperature (140 °C–160 °C). A total of 1.1 mmol (231 μL) of HMS mixed with 8 mL of ODE (sulfur precursor) was quickly injected into the reaction system. The reaction solution was annealed at that temperature for 3 h under argon flow. The sample aliquots were collected at different times during annealing, to obtain different size variations. After 3 h, the solution was cooled naturally to room temperature by removing the reaction flask from the heating mantle. Samples were washed by centrifugation once with ethanol, followed by a toluene/ethanol mixture. Finally, the sample precipitation was dried and dispersed in anhydrous toluene. A similar approach has been followed to obtain AZTS nanocrystals using S-ODE as the sulfur precursor. In this approach, 1.1 mmol of elemental sulfur powder was dissolved in 8 mL of ODE by heating at high temperature (150 °C) and injected into the reaction mixture at 180 °C. In this process, we annealed the samples for 2 h at the injection temperature. For larger sized particles (9.3 nm) the reaction temperature was raised to 190 °C and maintained for 2.5 h.

Surface Passivation by Zn Overcoating. It is well established that an inorganic shell over luminescent QDs enhances fluorescence lifetime and PLQY by shielding the core and passivating the surface traps.^{25,26} Zn-oleate (0.4 M) was used to passivate the surface of the nanocrystals. In a typical synthesis, 0.22 g of $\text{Zn}(\text{OAc})_2 \cdot 2\text{H}_2\text{O}$, 1.6 mL of OA, and 4 mL of ODE were taken in a 25 mL round-bottom flask connected to a Schlenk line. The reaction mixture was degassed at 50 °C for 45 min under vigorous stirring. The temperature was then

increased to 180 °C under Ar atmosphere. The reaction mixture forms a clear solution as soon as it reach high temperature. Finally, the reaction was cooled down, and the Zn-oleate complex was collected and stored in a degassed vial under Ar atmosphere.

AZTS QDs synthesized using the above-described procedure were overcoated using the Zn-oleate after the desired size was achieved. In our experiment, we have overcoated the largest sized nanocrystals obtained from both the procedures (AZTS QDs, synthesized using HMS-ODE at 160 °C for 180 min and using S-powder in ODE at 180 °C for 120 min). In a typical synthesis, after the desired size is achieved, the reaction mixture was cooled down to 140 °C and 800 μL of Zn-oleate was dropwise added into the reaction mixture. The reaction mixture was then maintained at that temperature for 20 min. Finally, the nanocrystals were cooled down to room temperature and washed by centrifugation using a toluene/ethanol mixture three times and redispersed in toluene. This Zn-oleate overcoating might result in formation of a very thin ZnS layer as a shell on AZTS QDs; however, it is nontrivial to characterize it due to its extremely small thickness (atomic layer).

Characterization. Transmission electron microscopy (TEM) was carried out at Centres Científics i Tecnològics de la Universitat de Barcelona (CCiT-UB) using a JEOL 2100 microscope using a field emission gun (FEG) operating at an acceleration voltage of 200 kV. X-ray diffraction patterns for the NQDs were recorded on a PANalytical X-pert PRO MPD Alpha1 diffractometer using $\text{Cu K}\alpha$ ($\lambda = 1.5406 \text{ \AA}$) radiation. Absorption spectra of samples were recorded using a Carry 5000 UV-vis-NIR spectrophotometer while steady-state and time-resolved PL spectra were obtained using a Horriba PL1057 spectrophotometer. Relative quantum yields were calculated with respect to Rhodamine 6G dye. Raman spectroscopy measurement were carried out on a Renishaw InVia spectrometer using a 532 nm laser at room temperature. An objective lens (50 \times) was used to focus the lasers on the samples. Elemental analysis of the samples was carried out using an inductively coupled plasma optical emission spectroscopy (ICP-OES) PerkinElmer, model Optima 3200RL, in

standard conditions. Samples for XPS were prepared on an ITO substrate by spin coating the AZTS QD solution followed by performing ligand exchange using tetrabutylammonium iodide (TBAI, 5 mg/mL) and 1,2-ethanedithiol (EDT, 1%). X-ray photoelectron spectroscopy (XPS) measurements were performed at the Institut Català de Nanociència i Nanotecnologia (ICN2) with a Phoibos 150 analyzer (SPECS) in ultrahigh-vacuum conditions (base pressure of 1×10^{-10} mbar) equipped with a monochromatic $K\alpha$ X-ray source (1486.74 eV). The pass energy value used was 10 eV for the high-resolution spectrum. Intensities were estimated by calculating the integral of each peak, determined by subtracting the Shirley-type background and fitting the experimental curve to a combination of Lorentzian and Gaussian lines of variable proportions.

Device Fabrication and Characterization. A 50 mg/mL solution of AZTS QDs (7 nm) in toluene was spin coated on ITO films with a speed of 2500 rpm for 30 s followed by a few drops of EDT (1%) dissolved in acetonitrile. The ligand was left to react for 10 s prior to dispensing a flush of acetonitrile and a flush of toluene. Thus, by a layer-by-layer process the desired film thickness (240 nm) was obtained. Finally, 3 nm MoO_3 and 100 nm Ag was deposited using a shadow circular mask of 2 mm in diameter. The devices were annealed at 120 °C in air for 15 min. Both current–voltage characteristics and transient photoresponse measurements were performed using a Keithley 2400 source-measuring unit under dark and 72 mW/cm^{-2} 637 nm laser illumination.

RESULTS AND DISCUSSION

We have synthesized AZTS colloidal QDs by hot injection of S precursor into the cationic precursor as described in above. We have carefully monitored the reaction temperature and annealing time to obtain a series of different sizes of AZTS QDs as manifested by the TEM images shown in Supporting Information Figure S1a–e. Average sizes and standard deviations obtained from the TEM analysis (Figure S2 and Table T1) as a function of the growth of the QDs range from 4.9 nm, 5.4 nm, 6.1 nm, and 6.5 nm to 6.9 nm, respectively. Higher reaction temperatures and longer annealing times lead to larger QD growth (Figure S1).

UV–vis absorption and PL spectroscopy (Figure 1a) shows the band gap tunability offered through the quantum size effect. The qualitative differences in the absorption and PL spectra with the growth of the particles are shown in Figure 1a. By tuning the QD size from 4.9 to 6.9 nm the PL emission peak of the QDs shifts from 740 to 850 nm. We also note the emergence of an exciton peak in the absorption spectra upon decreasing size of the nanocrystals, which becomes more evident in the case of 4.9 nm sized QDs. The optical band gap of the QDs has also been determined considering the Tauc equation ($(\alpha h\nu)^2$ vs $h\nu$, where α is absorption coefficient, h is Planck's constant, and ν is frequency) shown in Figure 1b. Here we consider AZTS as a direct band gap semiconductor because, from the theoretical calculation of band structure (shown in Figures S3 and S4) and from previous literature based on AZTS,^{21,27,28} it is evident that the conduction band minima and valence band maxima lie on the same k-point (Γ). The band gap can be tuned from a confined value of 1.65 eV (4.9 nm diameter) to 1.48 eV (6.9 nm diameter), reaching the bulk band gap of AZTS²² (see also Figures S3 and S4, for density functional theory (DFT) calculations of the bulk electronic properties of AZTS). Typically multinary QDs like I–III–VI type semiconductor QDs (CuInS_2 , AgInS_2 , CuInSe_2 , AgInSe_2) exhibit a broad PL emission (with fwhm of 300 meV or higher) and a large Stokes shift because of the recombination of the photogenerated carrier through optically active midgap states formed due to structural disorders or

defects. On the contrary, in the case of AZTS presented here, the PL emission peaks are comparatively narrower (fwhm less than 250 meV) with very small Stokes shift, and the PL emission peak energy overlaps with the measured band gap from the absorption Tauc plot. This effect has been reported previously in bulk $\text{Ag}_2\text{ZnSnSe}_4$ and $\text{CuBaSn}(\text{SSe})_4$ thin films.^{21,29–31} This suggests that AZTS QDs have shallow defect states which are optically active and emit very close to the band edge compared to previously reported multinary QDs and do not have significant band tailing effects in this semiconductor system.²⁰ To verify that the band gap tunability is through the quantum size effect and not due to stoichiometric modification of the composition,^{29,32} we performed inductively coupled plasma optical emission spectroscopy (ICP-OES) as tabulated in Table T2 that shows the preservation of a similar stoichiometry among QDs of different band gaps. Moreover, we observed (Table T3 and Figure S5) that a small variation in stoichiometry (1–2%) of the same sized dots does not affect the band gap of the QDs.

Typical variation of the band gap of AZTS nanocrystals as a function of size is shown in Figure 1c. In order to estimate the Bohr diameter of this semiconductor and the theoretically predicted band gap size dependence thereof, we performed theoretical calculations. The theoretical confinement energy ($\Delta E = \hbar^2\pi^2/2\mu r^2$) is calculated considering a spherical potential of radius r , and μ is the reduced mass (0.183 m_0 obtained from dispersion of bands) of exciton.³³ The theoretically calculated band gap variation with the size comes in good agreement with the experimental data (Figure 1c). The electronic structure of the AZTS (Figure S4a) confirms that the upper valence band is formed predominantly by Ag and S while the lower conduction band has a dominant contribution from Sn and S. Effective masses of electrons and holes were calculated from the dispersion of bands, while the dielectric constant was calculated from density functional perturbation theory. Within the effective mass approximation, we have determined the excitonic Bohr diameter for AZTS QDs to be 5.82 nm.

Long-term structural, optical, and colloidal stability is one crucial factor for the application of QDs, which is mostly limited by degradation of the QDs' surface. To improve the structural, optical, and colloidal stability we passivate the AZTS QDs using a thin inorganic as a protecting shell. DFT calculations of the density of states (DOS) show (Figure S4b,c) that, among the three cations, Zn contributes the least in both conduction and valence bands and therefore its presence on the surface would be expected to have the least effect in the optoelectronic properties of the QDs. We have thus developed a postsynthetic Zn-oleate capping of the AZTS QDs (see Experimental Methods section in the SI for details). Our experimental optical absorption and PL data (Figure 1d) show that upon Zn passivation the absorption spectra and the band gap remains almost the same as the pristine QDs while the TEM analysis shows the size is almost similar as shown in Figures S1f and S2f. The PL quantum yield (Figure 1d) drastically improves (Table T2) upon Zn shelling, and the PL lifetime (Figure 1e) is prolonged by a factor of 4. The use of Zn-oleate as a passivant has also been reported in other ternary chalcogenide QD systems.^{26,34} However, the PLQY of these QDs is low (3.8%) compared to the established (Cd, Pb) based binary or (Cu, In) based ternary chalcogenide QDs. While Zn-oleate has been used here to passivate the surface resulting in improvement of PLQY, there could be other

reasons behind these low PLQYs, for example (i) the presence cationic disorder resulting in bulk defects which can act as nonradiative recombination centers, and (ii) “insufficient ligand passivation” as we have used solely oleic acid which may reduce the QY yet enables easy ligand exchange for optoelectronically active QD films.

We now turn to the structural and analytical characterization of the AZTS QDs. Low magnification TEM images show (Figure S1) that the particles are nearly spherical in nature. Figure 2a–e shows the high resolution TEM (HRTEM)

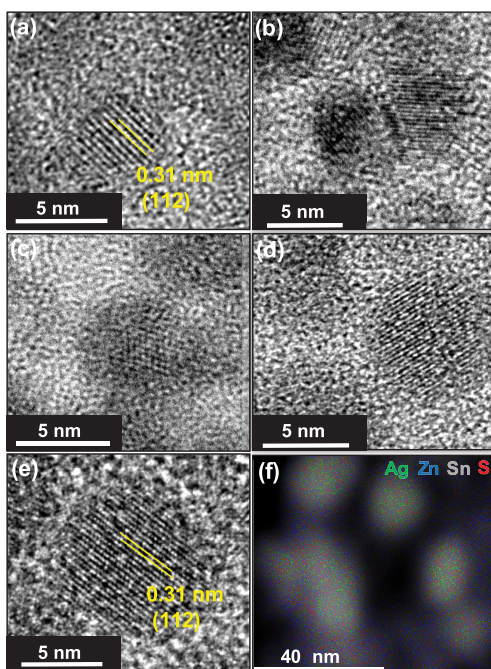


Figure 2. Representative HRTEM images of (a) 4.9 nm, (b) 5.4 nm, (c) 6.1 nm, (d) 6.5 nm, and (e) 6.9 nm AZTS QDs. (f) STEM-EDS elemental mapping of 6.9 nm AZTS QDs.

images of various sizes of NCs. The clear lattice fringes reveal the high quality crystalline nature of all the QDs. The observed 0.31 nm lattice fringe width from HRTEM images matches well with the (112) crystallographic planes. Figure 2f shows the scanning transmission electron microscope (STEM)-EDS elemental mapping where all the elements are superimposed on the dark field image. From the spatial distribution of Ag, Zn, Sn, and S it is apparent that all the elements are distributed uniformly throughout the crystals with no evidence of phase segregation among the QDs.

In order to identify the crystal structure and compositional purity of these QDs we employed X-ray diffraction (XRD) and Raman spectroscopy. Figure 3a shows the XRD patterns for different sized AZTS QDs as well as Zn-oleate passivated 6.9 nm diameter AZTS QDs. Due to the very small size of the QDs, the diffraction peaks are broad; however, the diffraction pattern matches with kesterite-phase CZTS (ICSD 171983). Moreover, a small shift in lower angles compared to the standard CZTS bulk data, as observed in the figure, is due to the larger cation size of Ag^+ compared to Cu^+ that modifies the lattice parameter as well as the interplanar spacing. XRD data alone cannot conclusively determine the phase purity of quaternary QDs, due to their similarity with binary and ternary potentially existing byproducts with similar crystal structure.¹⁴

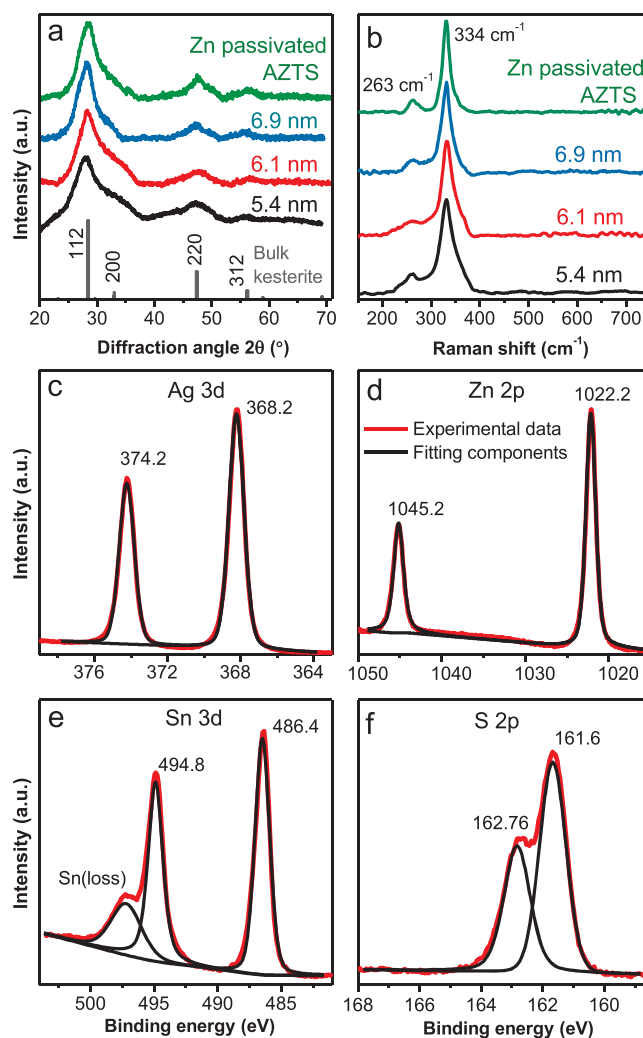


Figure 3. (a) XRD patterns and (b) Raman spectra of AZTS QDs of different sizes and Zn-oleate passivated AZTS. High resolution XPS of 6.9 nm AZTS QDs demonstrating (c) Ag 3d, (d) Zn 2p, (e) Sn 3d, and (f) S 2p peaks.

We therefore verified the phase purity of our NCs using Raman spectroscopy. Raman spectra of both AZTS and Zn-oleate passivated AZTS QDs in Figure 3b show that the peaks at 265 and 334 cm^{-1} are in good agreement with the vibrational mode of bulk AZTS (RRUFFID: R061016). The broadening of the Raman peak for the QDs that has been observed in our experimental data is due to the phonon confinement inside the QDs. Raman spectra do not present any other secondary peaks of impurities such as ZnS , Ag_2S , or SnS , which indicates the pure phase formation of AZTS NCs.

Furthermore, to study the phase stability over time, the QDs were stored in ambient conditions for 2 months and then subjected to Raman mapping. The overall intensity at the 334 cm^{-1} peak as displayed in Figure S6a–d suggests that surface passivated QDs are more stable than the bare QDs. Figure S6e,f shows the recorded Raman spectra corresponding to the marked points in Figure S6c,d. There is a clear change in the spectral feature (Figure S6e) that indicates the formation of an impurity or other phase in the case of bare AZTS while the clear signal (Figure S6f) without any other impurity feature suggests the superior phase stability of Zn-oleate passivated QDs.

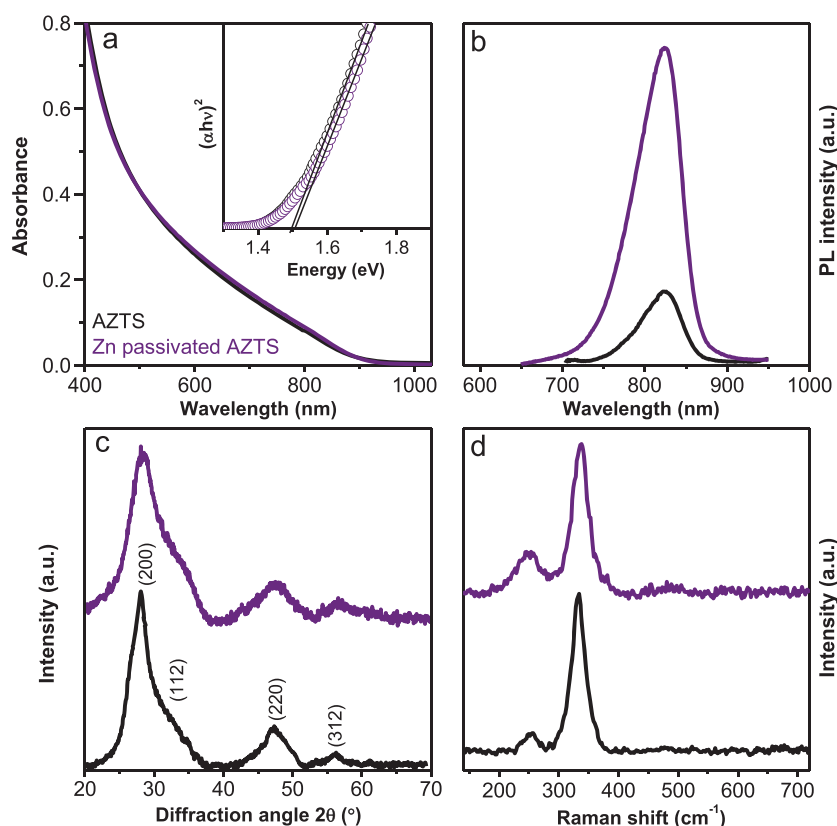


Figure 4. (a) Absorption, (b) photoluminescence spectra, (c) XRD diffraction pattern, and (d) Raman spectra of pristine AZTS (black) and Zn-oleate passivated AZTS (dark violet) QDs synthesized at 180 °C using S-ODE as the sulfur source. Inset of part (a) shows the Tauc plot showing band gaps of 1.5 eV for both the QDs.

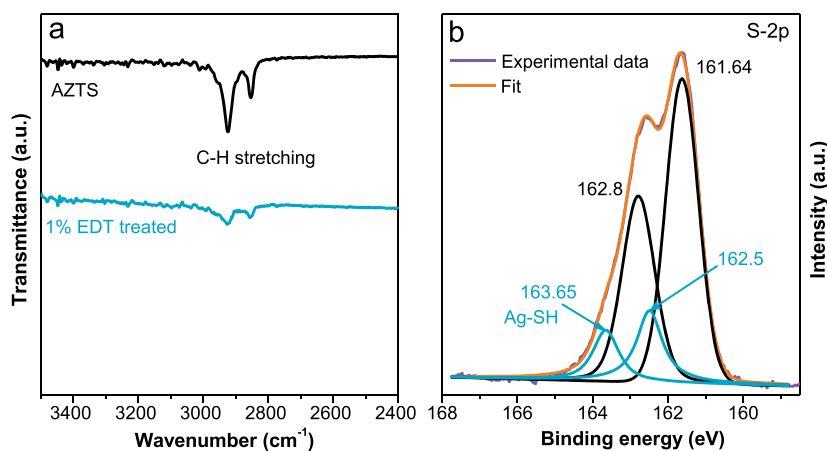


Figure 5. (a) FTIR spectra of AZTS films before and after ligand treatment. (b) High resolution XPS spectra, demonstrating S-2p peaks for EDT treated AZTS QDs.

XPS analysis has also been performed to investigate the surface and the subsurface chemical states of the constituent element in AZTS QDs. An overview of the spectrum (Figure S7) of the AZTS QDs synthesized at 160 °C confirms the presence of Ag, Zn, Sn, O, C, and I. Figure 3c–f represents the high resolution XPS spectra around Ag 3d, Zn 2p, Sn 3d, and S 2p, respectively. The ratio between the integrated intensity of Ag 3d/Zn 2p/Sn 3d/S 2p = 2:1.3:1.2:2.5 which suggests that the surfaces of these QDs are cation rich. However, for further information the spectra have been deconvoluted considering the spin orbit splitting where the binding energy differences, full width at half maximum (fwhm), and area under the curve

are fixed with standard database literature. It is evident from Figure 3c that the binding energies of Ag 3d_{5/2} and Ag 3d_{3/2} are located at 368.2 and 374.2 eV, respectively, with a peak splitting at 6 eV. The Zn 2p peaks split into binding energies of 1022.2 (Zn 2p_{3/2}) and 1045.2 (Zn 2p_{1/2}) with a peak splitting of 23 eV likely due to the formation of Zn²⁺ as shown in Figure 3d. The tin core level spectrum (Figure 3e) can be deconvoluted into two doublet peaks located at 486.4 eV (3d_{5/2}) and 494.8 eV (3d_{3/2}) with a peak splitting of 8.4 eV, indicating the presence of the Sn⁴⁺ valence state. Furthermore, we observe a broad peak with the higher binding energy side of the 3d_{3/2} spin–orbit component as shown in Figure 3e. This is

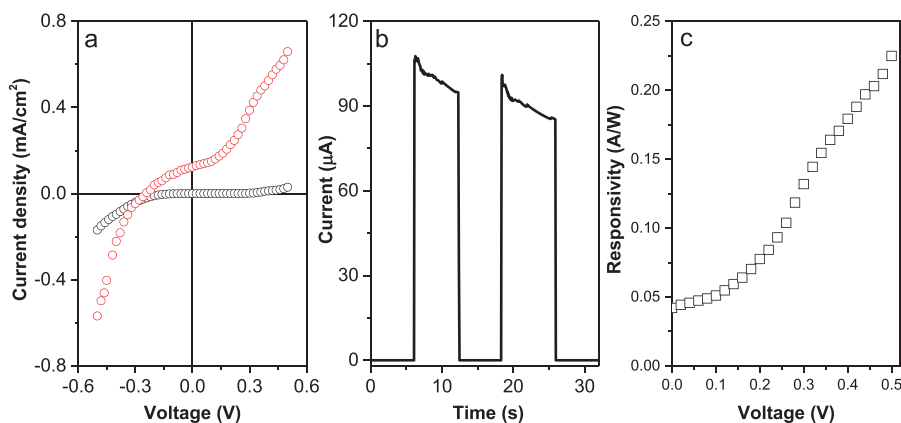


Figure 6. (a) Current–voltage characteristics of the ITO/AZTS QDs 240 nm/MoO₃-Al device and (b) photoresponse of the device with an interlay of dark and laser (635 nm) illumination. (c) Variation of responsivity over applied bias.

likely due to the Sn loss feature observed earlier.^{35,36} In the S 2p spectrum (Figure 3f), the deconvoluted doublet peaks are located at 161.6 and 162.76 eV with a peak separation of 1.16 eV, consistent with the expected S in the sulfide phase.

HMS, albeit highly reactive, is expensive; we therefore sought to replace HMS with elemental sulfur as the sulfur source. Due to the lower reactivity of the sulfur–ODE complex, we performed the synthesis at a slightly elevated temperature (180, 190 °C) followed by Zn-oleate treatment to passivate the surface. Thereby, we obtained larger sized QDs (pristine AZTS 7.7 nm, 9.3 nm and Zn-oleate passivated AZTS 7.9 nm) as shown in the TEM image in Figure S8. The optical properties show similar absorption and PL natures (Figure 4a,b) as observed before. XRD and Raman analysis confirms the formation of pure phase AZTS QDs as shown in Figure S10. Similar to synthesis using HMS, we also observed improved phase and optical stability upon Zn passivation in these QDs. We do not witness any further red shift in absorption or PL emission which indicates the particle size reaches to the bulk regime where it does not show any confinement effect.

The use of oleate ligands enables the employment of ligand exchange processes toward optoelectronically active QD films. In order to show the easy replacement of a long chain organic ligand attached to the AZTS QDs with short chain inorganic ligand, solid-state ligand exchange was performed during film formation. Evidence of successful solid-state ligand exchange on films has been shown by studying the surface ligand environment via Fourier transformed infrared (FTIR) spectroscopy and XPS (Figure 5). As-synthesized oleic acid capped AZTS films were treated with various thiols (1% of 1,2-ethanedithiol (EDT) dissolved in acetonitrile). The significant reduction of C–H stretching in after thiol treatment suggests the successful ligand exchange on these QDs as shown in Figure 5a. It is worth noting that the existence of small C–H stretching after thiol treatment is due to the C–H bond present in thiols. Furthermore, we have studied the surface chemistry after ligand exchange on nanocrystals using XPS spectroscopy. A comparison of S 2p high-resolution XPS spectra between the iodide (Figure 3f) and thiol treated (Figure 5b) nanocrystals shows the presence of bound metal–SH peaks in thiol treated samples due to the successful replacement with the thiol ligand.

Finally, photoconductivity of thin films of ligand exchanged AZTS QDs has been measured on a device in which a 240 nm

AZTS QD film is sandwiched between ITO and the MoO₃–Ag metal layer. *J*–*V* characteristics show (Figure 6a) that the AZTS QD film acts as a photodiode under 637 nm laser illumination with fast photoresponse and responsivity of 0.042 A/W at short circuit conditions (Figure 6b,c). These findings demonstrate the potential of these QDs as an optoelectronically active material for photovoltaic application.

CONCLUSION

In summary, a synthetic method for producing size controlled, luminescent environmentally friendly AZTS QDs has been developed and reported for the first time. We demonstrate for the first time the quantum confinement effect in these quaternary QDs. Additionally, we have shown that passivation of the AZTS surface using Zn-oleate improves the colloidal and phase stability in ambient conditions and enhances the PLQY. Moreover this work provides amine and thiol free AZTS QDs, stabilized only in oleic acid as ligand which can be readily exchanged with short chain ligands paving the way for their adoption in optoelectronic device applications.

ASSOCIATED CONTENT

Supporting Information

The Supporting Information is available free of charge at <https://pubs.acs.org/doi/10.1021/acs.chemmater.9b05370>.

Details of theoretical calculations and computational details, TEM images, and size distribution; UV–vis absorption, photoluminescence, Raman mapping, and XPS overview of AZTS QDs (PDF)

AUTHOR INFORMATION

Corresponding Author

Gerasimos Konstantatos – ICFO-Institut de Ciències Fotòniques, The Barcelona Institute of Science and Technology, 08860 Castelldefels, Barcelona, Spain; ICREA-Institució Catalana de Recerca i Estudis Avançats, 08010 Barcelona, Spain; orcid.org/0000-0001-7701-8127; Email: gerasimos.konstantatos@icfo.es

Authors

Avijit Saha – ICFO-Institut de Ciències Fotòniques, The Barcelona Institute of Science and Technology, 08860 Castelldefels, Barcelona, Spain

Alberto Figueroba – ICFO-Institut de Ciències Fotòniques, The Barcelona Institute of Science and Technology, 08860 Castelldefels, Barcelona, Spain

Complete contact information is available at:
<https://pubs.acs.org/10.1021/acs.chemmater.9b05370>

Notes

The authors declare no competing financial interest.

ACKNOWLEDGMENTS

The authors acknowledge financial support from the European Research Council (ERC) under the European Union's Horizon 2020 research and innovation programme (Grant Agreement No. 725165), the Spanish Ministry of Economy and Competitiveness (MINECO), and the "Fondo Europeo de Desarrollo Regional" (FEDER) through Grant TEC2017-88655-R. The authors also acknowledge financial support from Fundacio Privada Cellex, the program CERCA, and the Spanish Ministry of Economy and Competitiveness through the "Severo Ochoa" Programme for Centres of Excellence in R&D (SEV-2015-0522).

REFERENCES

- (1) Xu, J.; Voznyy, O.; Liu, M.; Kirmani, A. R.; Walters, G.; Munir, R.; Abdelsamie, M.; Proppe, A. H.; Sarkar, A.; García de Arquer, F. P.; Wei, M.; Sun, B.; Liu, M.; Ouellette, O.; Quintero-Bermudez, R.; Li, J.; Fan, J.; Quan, L.; Todorovic, P.; Tan, H.; Hoogland, S.; Kelley, S. O.; Stefiak, M.; Amassian, A.; Sargent, E. H. 2D Matrix Engineering for Homogeneous Quantum Dot Coupling in Photovoltaic Solids. *Nat. Nanotechnol.* **2018**, *13* (6), 456–462.
- (2) Pietryga, J. M.; Park, Y.-S.; Lim, J.; Fidler, A. F.; Bae, W. K.; Brovelli, S.; Klimov, V. I. Spectroscopic and Device Aspects of Nanocrystal Quantum Dots. *Chem. Rev.* **2016**, *116* (18), 10513–10622.
- (3) Kramer, I. J.; Sargent, E. H. The Architecture of Colloidal Quantum Dot Solar Cells: Materials to Devices. *Chem. Rev.* **2014**, *114* (1), 863–882.
- (4) Bernechea, M.; Miller, N. C.; Xercavins, G.; So, D.; Stavrinadis, A.; Konstantatos, G. Solution-Processed Solar Cells Based on Environmentally Friendly AgBiS₂ Nanocrystals. *Nat. Photonics* **2016**, *10*, 521.
- (5) Sandroni, M.; Wegner, K. D.; Aldakov, D.; Reiss, P. Prospects of Chalcopyrite-Type Nanocrystals for Energy Applications. *ACS Energy Lett.* **2017**, *2* (5), 1076–1088.
- (6) Du, J.; Du, Z.; Hu, J.-S.; Pan, Z.; Shen, Q.; Sun, J.; Long, D.; Dong, H.; Sun, L.; Zhong, X.; Wan, L.-J. Zn–Cu–In–Se Quantum Dot Solar Cells with a Certified Power Conversion Efficiency of 11.6%. *J. Am. Chem. Soc.* **2016**, *138* (12), 4201–4209.
- (7) Houck, D. W.; Siegler, T. D.; Korgel, B. A. Predictive Modeling of CuInSe₂ Nanocrystal Photovoltaics: The Importance of Band Alignment and Carrier Diffusion. *ACS Appl. Energy Mater.* **2019**, *2* (2), 1494–1504.
- (8) Kwak, D.-H.; Ramasamy, P.; Lee, Y.-S.; Jeong, M.-H.; Lee, J.-S. High-Performance Hybrid InP QDs/Black Phosphorus Photodetector. *ACS Appl. Mater. Interfaces* **2019**, *11* (32), 29041–29046.
- (9) Coughlan, C.; Ibáñez, M.; Dobrozhan, O.; Singh, A.; Cabot, A.; Ryan, K. M. Compound Copper Chalcogenide Nanocrystals. *Chem. Rev.* **2017**, *117* (9), 5865–6109.
- (10) Cui, X.; Sun, K.; Huang, J.; Lee, C.-Y.; Yan, C.; Sun, H.; Zhang, Y.; Liu, F.; Hossain, M. A.; Zakaria, Y.; Wong, L. H.; Green, M.; Hoex, B.; Hao, X. Enhanced Heterojunction Interface Quality To Achieve 9.3% Efficient Cd-Free Cu₂ZnSnS₄ Solar Cells Using Atomic Layer Deposition ZnSnO Buffer Layer. *Chem. Mater.* **2018**, *30* (21), 7860–7871.
- (11) Clarke, M. T.; Viscomi, F. N.; Chamberlain, T. W.; Hondow, N.; Adawi, A. M.; Sturge, J.; Erwin, S. C.; Bouillard, J.-S. G.; Tamang, S.; Stasiuk, G. J. Synthesis of Super Bright Indium Phosphide Colloidal Quantum Dots Through Thermal Diffusion. *Commun. Chem.* **2019**, *2* (1), 36.
- (12) Yarema, O.; Yarema, M.; Wood, V. Tuning the Composition of Multicomponent Semiconductor Nanocrystals: The Case of I–III–VI Materials. *Chem. Mater.* **2018**, *30* (5), 1446–1461.
- (13) Steinhagen, C.; Panthani, M. G.; Akhavan, V.; Goodfellow, B.; Koo, B.; Korgel, B. A. Synthesis of Cu₂ZnSnS₄ Nanocrystals for Use in Low-Cost Photovoltaics. *J. Am. Chem. Soc.* **2009**, *131* (35), 12554–12555.
- (14) Riha, S. C.; Parkinson, B. A.; Prieto, A. L. Solution-Based Synthesis and Characterization of Cu₂ZnSnS₄ Nanocrystals. *J. Am. Chem. Soc.* **2009**, *131* (34), 12054–12055.
- (15) Ford, G. M.; Guo, Q.; Agrawal, R.; Hillhouse, H. W. Earth Abundant Element Cu₂Zn(Sn_{1-x}Ge_x)S₄ Nanocrystals for Tunable Band Gap Solar Cells: 6.8% Efficient Device Fabrication. *Chem. Mater.* **2011**, *23* (10), 2626–2629.
- (16) Pan, Z.; Mora-Seró, L.; Shen, Q.; Zhang, H.; Li, Y.; Zhao, K.; Wang, J.; Zhong, X.; Bisquert, J. High-Efficiency "Green" Quantum Dot Solar Cells. *J. Am. Chem. Soc.* **2014**, *136* (25), 9203–9210.
- (17) Xie, R.; Rutherford, M.; Peng, X. Formation of High-Quality I–III–VI Semiconductor Nanocrystals by Tuning Relative Reactivity of Cationic Precursors. *J. Am. Chem. Soc.* **2009**, *131* (15), 5691–5697.
- (18) Kattan, N. A.; Griffiths, I. J.; Cherns, D.; Fermín, D. J. Observation of Antisite Domain Boundaries in Cu₂ZnSnS₄ by Atomic-Resolution Transmission Electron Microscopy. *Nanoscale* **2016**, *8* (30), 14369–14373.
- (19) Bourdais, S.; Choné, C.; Delatouche, B.; Jacob, A.; Larramona, G.; Moisan, C.; Lafond, A.; Donatini, F.; Rey, G.; Siebentritt, S.; Walsh, A.; Denler, G. Is the Cu/Zn Disorder the Main Culprit for the Voltage Deficit in Kesterite Solar Cells? *Adv. Energy Mater.* **2016**, *6* (12), 1502276.
- (20) Gokmen, T.; Gunawan, O.; Todorov, T. K.; Mitzi, D. B. Band Tailing and Efficiency Limitation in Kesterite Solar Cells. *Appl. Phys. Lett.* **2013**, *103* (10), 103506.
- (21) Chagarov, E.; Sardashti, K.; Kummel, A. C.; Lee, Y. S.; Haight, R.; Gershon, T. S. Ag₂ZnSn(S, Se)₄: A Highly Promising Absorber for Thin Film Photovoltaics. *J. Chem. Phys.* **2016**, *144* (10), 104704.
- (22) Ma, C.; Guo, H.; Zhang, K.; Yuan, N.; Ding, J. Fabrication of p-type Kesterite Ag₂ZnSnS₄ Thin Films with a High Hole Mobility. *Mater. Lett.* **2017**, *186*, 390–393.
- (23) Sasamura, T.; Osaki, T.; Kameyama, T.; Shibayama, T.; Kudo, A.; Kuwabata, S.; Torimoto, T. Solution-phase Synthesis of Stannite-type Ag₂ZnSnS₄ Nanoparticles for Application to Photoelectrode Materials. *Chem. Lett.* **2012**, *41* (9), 1009–1011.
- (24) Nishi, H.; Nagano, T.; Kuwabata, S.; Torimoto, T. Controllable Electronic Energy Structure of Size-controlled Cu₂ZnSnS₄ Nanoparticles Prepared by a Solution-based Approach. *Phys. Chem. Chem. Phys.* **2014**, *16* (2), 672–675.
- (25) Saha, A.; Chellappan, K. V.; Narayan, K. S.; Ghatak, J.; Datta, R.; Viswanatha, R. Near-Unity Quantum Yield in Semiconducting Nanostructures: Structural Understanding Leading to Energy Efficient Applications. *J. Phys. Chem. Lett.* **2013**, *4* (20), 3544–3549.
- (26) So, D.; Konstantatos, G. Thiol-Free Synthesized Copper Indium Sulfide Nanocrystals as Optoelectronic Quantum Dot Solids. *Chem. Mater.* **2015**, *27* (24), 8424–8432.
- (27) Rasukkannu, M.; Velauthapillai, D.; Vajeeston, P. Hybrid Density Functional Study of Au₂Cs₂I₆, Ag₂GeBaS₄, Ag₂ZnSnS₄, and AgCuPO₄ for the Intermediate Band Solar Cells. *Energies* **2018**, *11* (12), 3457.
- (28) Rasukkannu, M.; Velauthapillai, D.; Vajeeston, P. Computational Modeling of Novel Bulk Materials for the Intermediate-Band Solar Cells. *ACS Omega* **2017**, *2* (4), 1454–1462.
- (29) Gershon, T.; Lee, Y. S.; Antunez, P.; Mankad, R.; Singh, S.; Bishop, D.; Gunawan, O.; Hopstaken, M.; Haight, R. Photovoltaic Materials and Devices Based on the Alloyed Kesterite Absorber (Ag_xCu_{1-x})₂ZnSnSe₄. *Adv. Energy Mater.* **2016**, *6* (10), 1502468.
- (30) Gershon, T.; Sardashti, K.; Gunawan, O.; Mankad, R.; Singh, S.; Lee, Y. S.; Ott, J. A.; Kummel, A.; Haight, R. Photovoltaic Device

with over 5% Efficiency Based on an n-Type $\text{Ag}_2\text{ZnSnSe}_4$ Absorber. *Adv. Energy Mater.* **2016**, *6* (22), 1601182.

(31) Teymur, B.; Zhou, Y.; Ngaboyamahina, E.; Glass, J. T.; Mitzi, D. B. Solution-Processed Earth-Abundant $\text{Cu}_2\text{BaSn}(\text{S},\text{Se})_4$ Solar Absorber Using a Low-Toxicity Solvent. *Chem. Mater.* **2018**, *30* (17), 6116–6123.

(32) Gershon, T.; Sardashti, K.; Lee, Y. S.; Gunawan, O.; Singh, S.; Bishop, D.; Kummel, A. C.; Haight, R. Compositional Effects in $\text{Ag}_2\text{ZnSnSe}_4$ Thin Films and Photovoltaic Devices. *Acta Mater.* **2017**, *126*, 383–388.

(33) Protesescu, L.; Yakunin, S.; Bodnarchuk, M. I.; Krieg, F.; Caputo, R.; Hendon, C. H.; Yang, R. X.; Walsh, A.; Kovalenko, M. V. Nanocrystals of Cesium Lead Halide Perovskites (CsPbX_3 , X = Cl, Br, and I): Novel Optoelectronic Materials Showing Bright Emission with Wide Color Gamut. *Nano Lett.* **2015**, *15* (6), 3692–3696.

(34) Li, L.; Pandey, A.; Werder, D. J.; Khanal, B. P.; Pietryga, J. M.; Klimov, V. I. Efficient Synthesis of Highly Luminescent Copper Indium Sulfide-Based Core/Shell Nanocrystals with Surprisingly Long-Lived Emission. *J. Am. Chem. Soc.* **2011**, *133* (5), 1176–1179.

(35) Wang, L.; Li, J.; Wang, Y.; Yu, K.; Tang, X.; Zhang, Y.; Wang, S.; Wei, C. Construction of 1D SnO_2 -coated ZnO Nanowire Heterojunction for their Improved n-Butylamine Sensing Performances. *Sci. Rep.* **2016**, *6* (1), 35079.

(36) Ju, D.-X.; Xu, H.-Y.; Qiu, Z.-W.; Zhang, Z.-C.; Xu, Q.; Zhang, J.; Wang, J.-Q.; Cao, B.-Q. Near Room Temperature, Fast-Response, and Highly Sensitive Triethylamine Sensor Assembled with Au-Loaded ZnO/ SnO_2 Core–Shell Nanorods on Flat Alumina Substrates. *ACS Appl. Mater. Interfaces* **2015**, *7* (34), 19163–19171.